Geophys. J. Int. (2000) **143,** 83–98

Permanent water level drop associated with the Spitak Earthquake: observations at Lisi Borehole (Republic of Georgia) and modelling

P. Gavrilenko,[1] G. Melikadzé,[2] T. Chélidzé,[3] D. Gibert[1] and G. Kumsiashvili[3]

[1] *Geosciences Rennes,* UPR 4661, *CNRS, Rennes, France*
[2] *Gruzgeologia, Tbilissi, Republic of Georgia*
[3] *Institute of Geophysics, Georgian Academy of Sciences, Tbilissi, Republic of Georgia*

Accepted 2000 April 20. Received 2000 April 18; in original form 1999 March 22

SUMMARY

We present the results of a series of measurements that were made between 1988 and 1992 at Lisi (Georgia). Water level variations in the Lisi well, barometric pressure, precipitation (including rain and snow) and temperature measurements were made during this period. A hydraulic 'slug test' has been performed more recently in the well. Two major seismic events occurred during the observation period in the Caucasus area. The Spitak seismic event of 1988 December 9, 110 km from the Lisi borehole, left a clear post-seismic hydraulic signature, whereas the second event, that of 1991 April 29, 125 km from the borehole, did not seem to induce any detectable anomaly. First, we analyse the tidal and barometric responses of the water level in order to calibrate the borehole and to determine the hydraulic parameters of the aquifer. Then we develop a model for aquifer recharge by meteoric precipitation. Finally, we compare our model with the observed water level variations in the well. We highlight anomalous behaviour that correlates with the earthquake, with the following characteristics: the water level drops about 75 cm with a time constant of 6.6 days. The initial water level is never recovered and the change appears permanent on the scale of the period of observation. Since it is delayed in time, the anomalous water level cannot be attributed to coseismic deformation. Following the suggestion of some authors that the observed behaviour could be related to damage of the aquifer due to the passage of seismic waves, we attempted to take this process into account and to model the resulting water level variations in the aquifer. A double porosity model (including fractures and a porous medium) has been used to describe the modifications undergone by the medium. The medium is discretized at two different scales—(1) at the scale of a porous block and (2) at the scale of the fractured system (which may include a finite number of porous blocks). Using this basic model we have tested three interpretative models: (1) a variable-permeability model; (2) a locally varying porosity model; (3) a model combining (1) and (2). We show that an increase in permeability by a factor of 2 is needed in order to describe the permanent water level drop, whilst the locally varying porosity zones account for the observed time constants of the anomaly. Using this model, simulations show that we are able to describe water level variation associated with precipitation for the whole period of observation.

Key words: earthquakes, fractures, hydrology, permeability, porosity.

1 INTRODUCTION

Water level recording in wells is one of the most effective methods of monitoring strain variations in the upper part of the Earth's crust. Despite intensive theoretical and experimental research (e.g. Roeloffs 1988; Roeloffs *et al.* 1989; Kumpel 1992; Muir-Wood & King 1993; Igarashi & Wakita 1991; Roeloffs & Quilty 1997) the relationship between the hydrological response and the crustal strain still cannot be interpreted in a straightforward way; the observed coseismic effects often do not agree with dislocation models at the earthquake source either in the magnitude or in the sign of the response.

Figure 1. Map of Georgia showing the locations of the station Lisi and the Spitak and Racha earthquakes.

In the present paper, we consider the results of water level monitoring in the Lisi borehole, which is part of the regional network of the Western Caucasus, which includes 12 stations. The well is situated in the Adjara–Trialeti Mountain tectonic zone; its coordinates are 41.45°N, 44.45°E (see Fig. 1) and its elevation is 692.65 m. The depth of the well is 330 m. The well cuts a sequence of clays, sandstones and argillites; it meets middle Eocene sandstone aquifers at depths of 30–67 and 170–250 m. The well is screened (perforated) between 30 and 200 m and the mean (stable) water level is recorded by mechanical GR-38 piezometers, manufactured in Russia and modified to attain higher sensitivity of the order of 1 cm. The hourly averaged data are picked up and collected into a database, containing more than 20 000 readings. Fig. 2 shows the variation of water level measured from the land surface. The meteorological data that are necessary for the interpretation have been taken from the database at the Hydrological Survey of Georgia. Thus, in addition to water level recordings, barometric pressure, temperature and precipitation (rain and snow cover) are available (Figs 3b–e respectively).

Well hydraulic heads respond to the following main strain-generating factors: earth tides, atmospheric pressure variations, tectonic (aseismic) and seismic events. The time dependence of hydraulic heads is a complicated function of the hydraulic conductivity of rocks, the scale of flow, the degree of confinement of the aquifer and other factors (Rojstaczer 1988).

Two major seismic events occurred in the Caucasus area during the observation period relatively close to the well: Spitak (1988 December 7, $M=6.8$, $\Delta=110$ km) and Racha (1991 April 29, $M=6.9$, $\Delta=125$ km), where M is the magnitude and Δ is the epicentral distance. Fig. 1 shows the locations of the epicentres of the two earthquakes. The post-seismic hydraulic signature is particularly clear after the Spitak event (see Fig. 2). To interpret those effects it is necessary to know the main parameters of the aquifer, that is, its hydraulic conductivity K, its specific storativity S_s, the strain sensitivity of the well (i.e. fluid elevation versus strain) and the degree of confinement of the aquifer. In order to assess these parameters we analyse the tidal, barometric and pluviometric responses of the water level. In addition, in order to check the results derived, hydraulic tests were performed at the Lisi borehole in July 1997. Finally, we develop a simple model to describe the possible relationship between fluid elevation variations and earthquake-related processes.

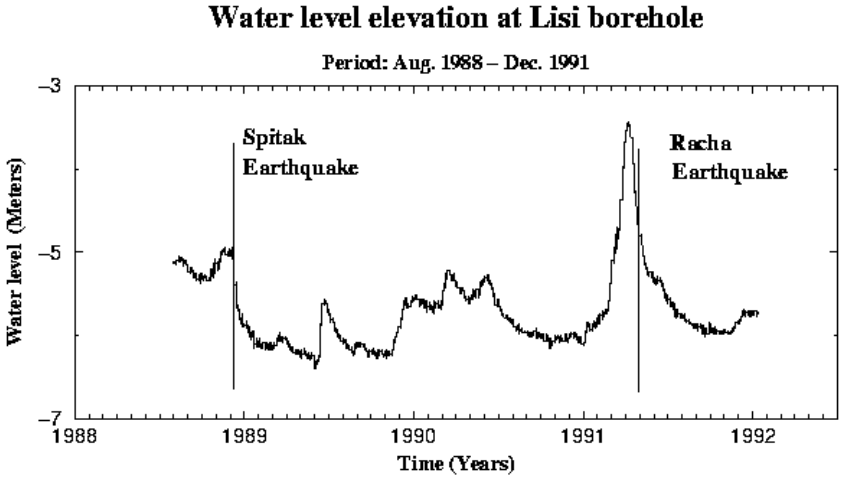

Figure 2. Water level variation at Lisi borehole for 3.5 yr of observations. Vertical lines show the occurrence times of the Spitak (1988 December 8) and Racha earthquakes (1991 April 29).

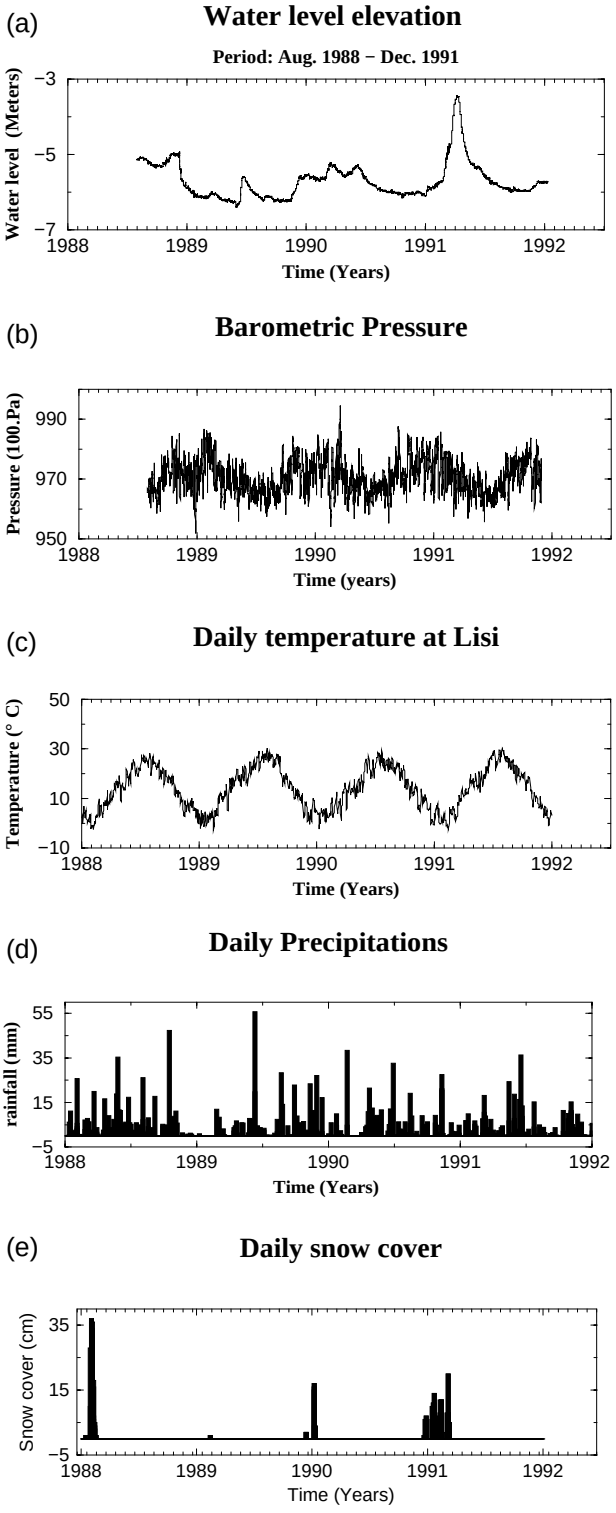

Figure 3. (a) Water level at Lisi, (b) atmospheric pressure, (c) ground temperature, (d) daily precipitation and (e) daily snow cover.

2 DATA PROCESSING

2.1 Tidal analysis

Aquifer properties are commonly derived from Earth tides. Usually, well responses to tides and the frequency dependence of the tidal response can be analysed in terms of both aquifer properties (unknown) and well properties (known). These features have been extensively studied in the past by Bredehoeft (1967), Hsieh *et al.* (1987) and others. Table 1 summarizes the characteristics of the main tidal waves that may be observed around diurnal (Q1, O1, P1, K1) and semi-diurnal (N2, M2, S2, K2) frequencies.

Table 1. The main tidal components.

Nature	Description	Name	Frequency (cpd)
diurnal	larger lunar elliptic	Q1	0.8932441
	principal lunar diurnal	O1	0.9295357
	principal solar diurnal	P1	0.9972621
	luni-solar diurnal	K1	1.0027379
semi-diurnal	larger lunar elliptic	N2	1.895982
	principal lunar	M2	1.932274
	principal solar	S2	2.000000
	luni-solar	K2	2.005476

Fig. 4 shows the amplitude spectrum resulting from high-pass filtering. High-pass cut-off is set to 0.7 cycles per day (cpd). Diurnal ($\approx$1 cpd) and semi-diurnal ($\approx$2 cpd) waves can be observed from this plot. Notice, however, that Q1, P1, N2, K2 are not far above the noise level. On the other hand, both K1 (1 cpd) and S2 (2 cpd) are affected by barometric pressure and their amplitudes cannot be analysed without considering both tidal and barometric pressure signals.

Analysis of the frequency dependence of the tidal response allows us to estimate the hydraulic parameters of the aquifer. Indeed, fluid flow into the wellbore is controlled by the diffusion

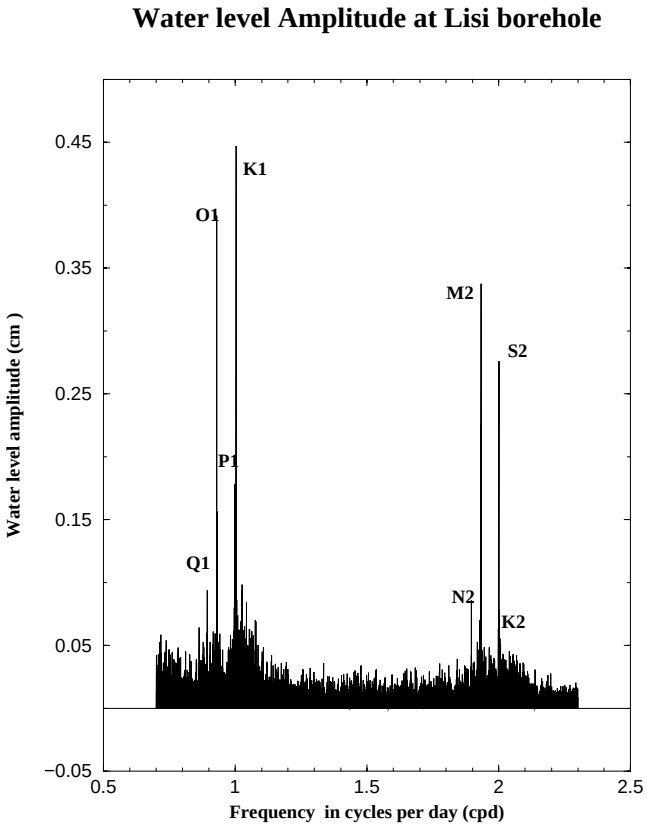

Figure 4. Amplitude spectrum of the signal.

time constant, which may be significant compared to the tidal wave period. This is likely to lead to amplitude attenuation and phase lag for high-frequency waves. In other words, the well/aquifer system acts as a filter. In order to determine the characteristics of this filter, the observed signal has to be compared to the input tide signal. As tidal measurements were not available, we used the theoretical tidal potential, calculated using the program RATGP95 (Roosbeek 1996). The amplitude ratio and phase lag between the observed and calculated tidal waves must be considered in order to highlight the frequency dependence of the response. The analysis of the tidal components was performed by applying non-dephasing narrow-band recursive filters centred on tidal frequencies for both theoretical and observed signals. The narrow-band filter induces undesirable effects at both edges of the filtered signal and consequently a corrective function that matches the envelope of the filtered signal is applied to rectify the signal. Finally, the average amplitude ratio, $|A_w/A_t|$, is calculated (A_w is the amplitude of the tidal signal and A_t is the amplitude of the theoretical signal). In addition, the phase delay, $(\phi_w - \phi_t)$, is determined using the Lissajou representation (again, the indices w and t denote the observed signal and the theoretical signal). We chose this procedure instead of least squares because it can more easily identify possible variations of the characteristics of the signal with time. However, we checked that both methods gave similar results.

We interpret the data on the basis of the theory developed by Hsieh *et al.* (1987). The response depends on the hydraulic as well as the geometrical parameters of the well. This was given by Hsieh *et al.* (1987) in the following form:

$$h(\omega) = h_0 \Psi(\alpha(\omega), \beta(\omega)), \quad (1)$$

where Ψ is a function in the complex plane that involves Kelvin functions of orders 0 and 1. $\alpha(\omega) = (\omega S_s/K)^{0.5} r_w$ and $\beta(\omega) = (\pi\omega r_c r_w)/(AK)$, in which r_c and r_w correspond respectively to the radius of the well where water level fluctuates and that where fluid penetrates, ω is the frequency of the harmonic oscillation and A is the area over which the well is open to the aquifer. As far as the Lisi well is concerned, $r_c = r_w = 0.127$ m and $A = 46.68$ m^2.

Only the waves that were not affected by barometric pressure were used. In addition, as seen before, Q1 and N2 are weak and do not provide a reliable estimate. Thus, we used only O1 and M2, which are strong enough to support reliable analysis. The results are shown in Fig. 5 together with the best fit obtained from eq. (1). We found that the strain sensitivity is around 27 cm/$\mu\varepsilon_0$, where ε_0 is the unit deformation. Accordingly, the product of the poroelastic parameter B (the Skempton coefficient) and K_u (undrained compressibility) is $BK_u = 2.7 \times 10^{11}$ Pa. The values of hydraulic conductivity and specific storativity that best fit the amplitude and phase lag are $K = 0.49 \times 10^{-6}$ m s^{-1} and $S_s = 0.14 \times 10^{-9}$ m^{-1}.

As noticed by Roeloffs *et al.* (1989), for a 1 per cent porosity aquifer the storativity should not be lower than 3×10^{-8} m^{-1}. Thus, although we do not know the exact value of porosity in these sandstones, it appears that the derived value for storativity is too low by at least two orders of magnitude. Since the area over which the well is open to the aquifer is not known accurately, this may be a source of error. Assuming an A-value of one-tenth of that used in the previous calculation leads to an increase of both hydraulic conductivity and storativity by one order of magnitude. Thus, although the estimation of A is certainly crude, it cannot explain the low value of S_s. We note that the water elevation response in the well does not depend strongly on storativity, as illustrated in Fig. 5. We report the amplitude and phase lag variations with frequency for two other sets of (K, S_s): ($K = 0.36 \times 10^{-6}$ m s^{-1}, $S_s = 0.56 \times 10^{-7}$ m^{-1}) and ($K = 0.30 \times 10^{-6}$ m s^{-1}, $S_s = 0.26 \times 10^{-6}$ m^{-1}), which we compare with the previous set ($K = 0.49 \times 10^{-7}$ m s^{-1}, $S_s = 0.14 \times 10^{-9}$ m^{-1}). The results are thus almost indistinguishable from the first set, even though storativity varies over more than three orders of magnitude. This shows that whilst K is rather well resolved, storativity cannot be reliably estimated using this method.

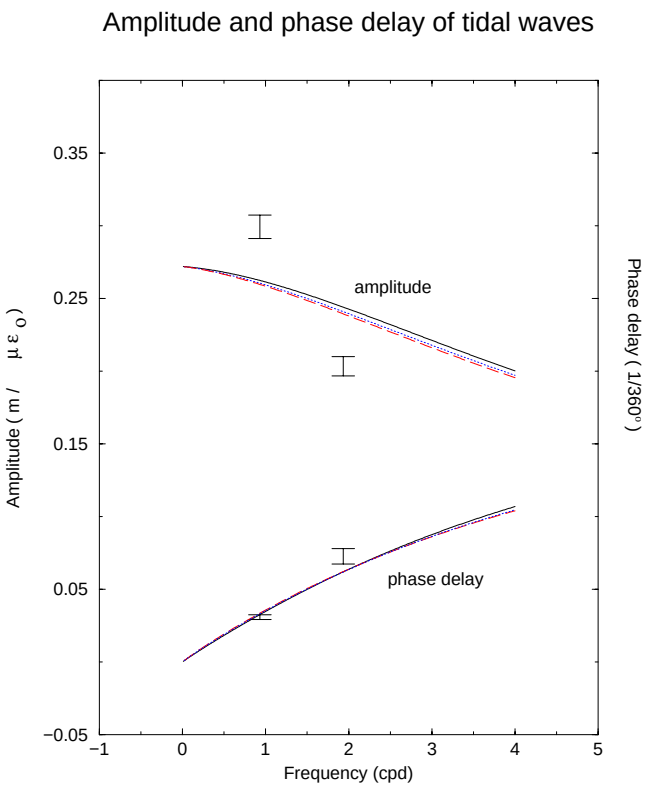

Figure 5. Amplitudes and phase delays of (01, M2) waves together with the best theoretical fit (solid line). The dotted and dashed lines correspond to two other sets of (K, S_s).

2.2 'Slug test' analysis

On the same well, we carried out a hydraulic (slug) test by adding a known volume (3 l) of water instantaneously and monitoring the return to the original head as water penetrated into the embedding media. The results of the field experiment are given in Fig. 6. The method used for the interpretation of the test data is based on the semi-logarithmic plot $h(t)/h_0$, as suggested by Hvorslev (1951) and Domenico & Schwartz (1990), where h_0 is the water level at $t = 0$, that is, at the beginning of the test. From Hvorslev (1951), the aquifer parameters are given by the following relation:

$$K = r_c^2 \ln(L/r_c)/(2LT_0), \quad (2)$$

where L is the thickness of the aquifer and T_0 is the time elapsed from the beginning of the test and for which $h(t)/h_0 = 0.37$ (see Fig. 6). In our case, one obtains $T_0 = 43.5$ min, which allows us to calculate $K = 1.8 \times 10^{-7}$ m s^{-1}. The Hvorslev method

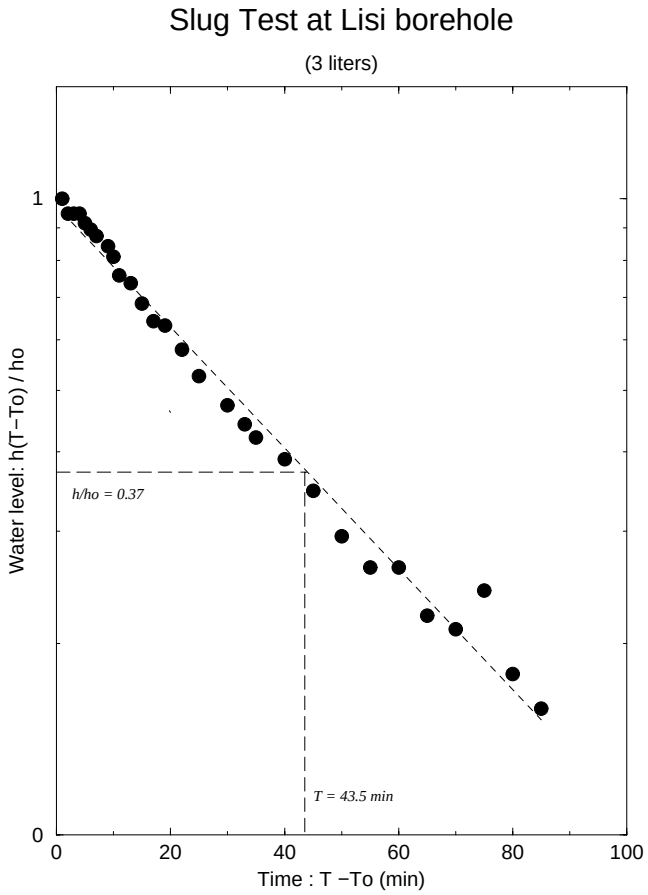

Figure 6. Normalized water level decline versus time (semi-log plot) after adding 3 l of water at time T_0 ('slug test').

is inappropriate for extracting storativity. However, this parameter is theoretically accessible through the method developed by Papadopoulos *et al* (1973). It consists of using calculated standard curves that are functions of two parameters that depend on K and S_s. However, these type curves do not match the experimental data very well. We found $K=3.4\times10^{-5}$ m s^{-1} and $S_s=1.0\times10^{-10}$ m^{-1}. Nevertheless, these results cannot be considered reliable. The important point to notice here is that the Hvorslev (1951) method yields a hydraulic conductivity very close (within a factor of 2 or 3) to the value obtained from the tidal wave inversion. This supports the results of the previous section.

2.3 Barometric analysis

In addition to the effect of tidal waves, barometric variations provide a second natural experiment that constrains the aquifer properties. Atmospheric pressure affects the pressure both in the well and in the aquifer, and one defines the barometric efficiency as the ratio between pressure variation within the aquifer and barometric pressure. Since barometric variation affects borehole pressure as well, water level variation in wells is related to barometric efficiency in the following way:

$$E_B=\rho g h/P_a\,, \tag{3}$$

where h is the water level variation and P_a is the change in barometric pressure. Let us consider fluid pressure P in the aquifer. E_B is then given by $(P_a-P)/P_a$. The transfer function in the frequency domain can be obtained by using the input/output cross-spectrum relation as described in Bendat & Piersol (1986). Since both barometric and tidal variations affect fluid elevation and contain both diurnal (1 cpd) and semi-diurnal (2 cpd) components, we are compelled to use a two-output model relation 7.22 of Bendat & Piersol (1986), as used by Rojstaczer (1988). Barometric efficiency is then given by

$$E_B(\omega)=\frac{BB(\omega)TW(\omega)-TB(\omega)BW(\omega)}{BB(\omega)TT(\omega)-BT(\omega)TB(\omega)}\,, \tag{4}$$

where the notation $XY(\omega)$ refers to the cross-spectrum between two signals $X(t)$ and $Y(t)$. Signals $B(t)$, $T(t)$ and $W(t)$ correspond respectively to barometric pressure, tides and water level records, so $BB(\omega)$ corresponds to the power spectrum of the barometric pressure, $BW(\omega)$ denotes the cross-spectrum between barometric pressure and water level, etc.

The dependence of barometric efficiency on frequency is due to fluid leakage into the unsaturated zone. Thus, frequency dependence provides indications of how the aquifer is confined. This dependence is given by the following relation Roeloffs & Quilty (1997):

$$E_B=-(1-\alpha)(1-A\exp\{-[i\omega(z_b-z_w)^2/c]^{1/2}\})\,, \tag{5}$$

where $\alpha=B(1+\nu_u)/3(1-\nu_u)$, ν_u is the undrained Poisson coefficient, $A=(\exp\{[i\omega(z_b-z_t)^2/c]^{1/2}\}-1)/[i\omega(z_b-z_t)^2/c]^{1/2}$, z_b is the depth of the bottom of the interval open to the aquifer, z_t is the depth of the top of the interval open to the aquifer, z_w is the depth of the water table and c is the vertical hydraulic diffusivity.

The inversion of aquifer parameters, namely α and c, can be performed from this equation. Since atmospheric pressure data are stored every 3 hr, the hourly water level data have been averaged accordingly. Atmospheric pressure data measured at the Lisi meteorological station are shown in Fig. 3(b). The barometric efficiency has been calculated over the entire period of water level monitoring using eq. (4). Following Bendat & Piersol (1986) (p. 400), spectral quantities are calculated on a block-by-block basis using time-series of 128 days length. A Fourier transform and a Hanning window were applied successively and then peaks of frequency of barometric pressure were extracted from the autospectral barometric signal. The barometric efficiency was then calculated at these frequencies as soon as they had been extracted more than once on the various blocks.

The results are shown in Fig. 7. Diamonds represent the calculated barometric efficiency and the solid line corresponds to the result of the inversion. Inversion based on eq. (5) gives $\alpha=0.29\pm0.04$ and $c=(4.4\pm1.2)\times10^{-2}$ m^2 s^{-1}. Assuming that the specific storativity takes the value $S_s=0.26\times10^{-6}$ (see Section 2.2), vertical hydraulic conductivity can be calculated: $K_{vert}=1.1\times10^{-8}$ m s^{-1}, that is, more than one order of magnitude less than the horizontal hydraulic conductivity. This gives an idea of how well the aquifer is confined. However, additional complexity makes this analysis questionable. As seen above, the well cuts two aquifers, which are likely to react differently to atmospheric pressure. This may partly explain the strong dispersion of the derived barometric pressure. We are not able to take this behaviour into account in our analysis. We show in Fig. 8 the first two months of recording corrected for the barometric pressure. For clarity, we applied a low-pass filter with a higher cut-off frequency of 0.7 cpd. Although the barometric pressure and water level recordings show anti-correlated

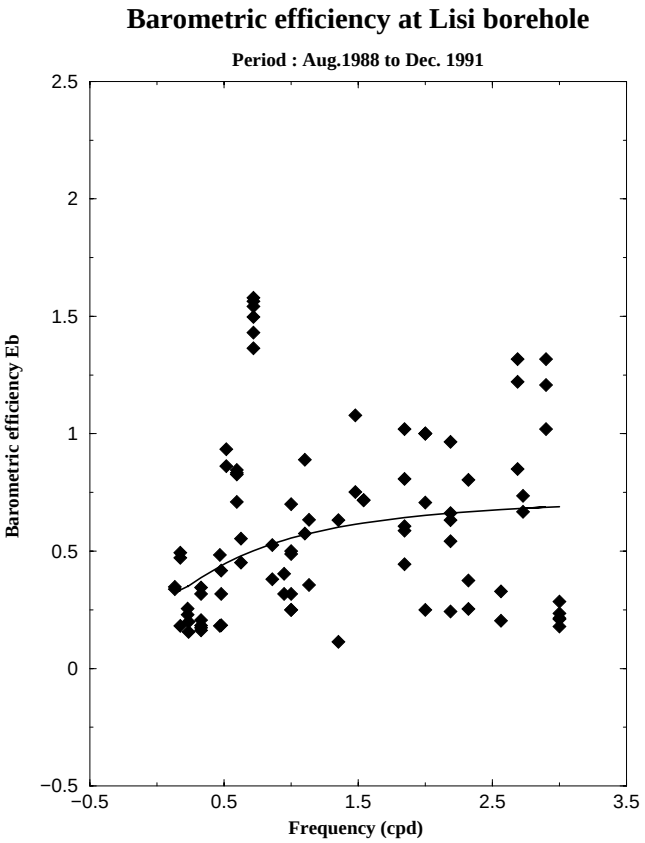

Figure 7. Barometric efficiency versus frequency. Diamonds correspond to calculated points. The solid line is the best theoretical fit.

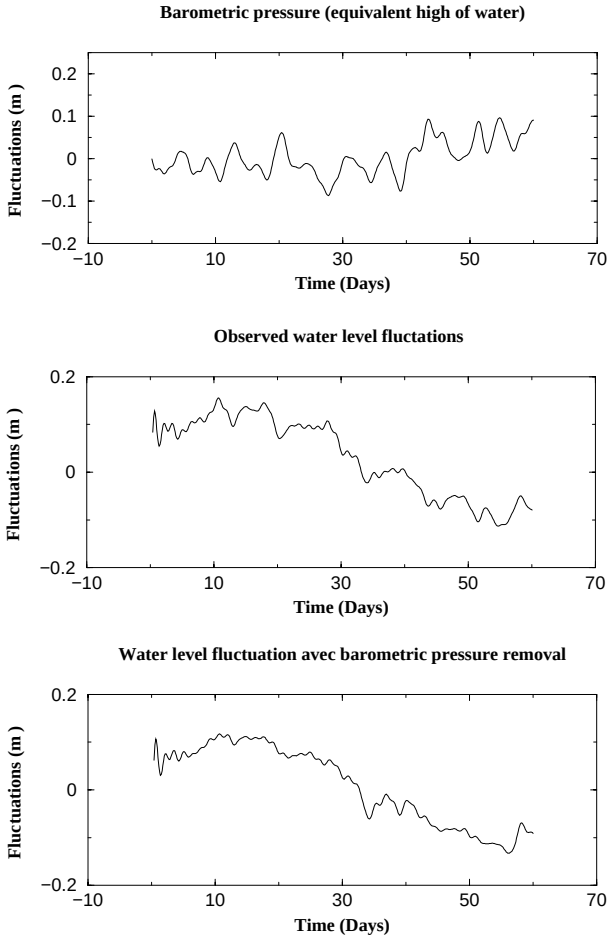

Figure 8. Water level fluctuation after removal of the barometric pressure response for the first 2 months of data with a low-pass cut-off frequency of 0.7 cpd.

peaks, they are, at least in part, removed in the corrected signal. Although the result is probably not perfect, it is sufficient for our purpose.

Another point to note here is that the amplitude of the signal does not vary much from frequencies around 1 cpd to frequencies around 2 cpd. Since this effect was not taken into account in the tidal analysis, the approximation is justified *a posteriori*.

2.4 Pluviometric analysis

In this section, we consider the recharge of the aquifer by precipitation. That implies a transfer function through the hydrologic system that must be determined. Our goal here is to analyse and quantify the effects related to the major earthquakes by comparing the expected and observed responses at the time of the earthquake. First, we need to estimate the infiltration rates using the rainfall records as a starting point. Second, these infiltration rates are used as input data and a transfer function is calculated.

The infiltration or effective rainfall concerns only the fraction of meteoric water that reaches the aquifer, thus it does not include rainfall run-off or water lost by evapotranspiration. The soil water budget is usually written as

$$S = P - E - T, \tag{6}$$

where S is the water surplus (that is, the quantity of water that infiltrates), P is precipitation, E is evaporation and T is the change in storage. T can be expressed as $\Delta W/\Delta t$, where W is the soil moisture and t is time. Note that rainfall run-off is not considered in the budget equation (6) or in the following. Indeed, we do not have a reliable estimate of this parameter.

Evapotranspiration obeys complex processes that take place in the soil. It is governed by the climatic conditions as well as by the soil properties. Thornthwaite (1948) provided a simple empirical approach to calculate water extracted from the soil by evapotranspiration and other approaches have since been developed. However, the former has the advantage of simplicity. It requires only the temperature and the estimate of day length as input parameters. First, the potential evapotranspiration PE (which refers to the maximum rate of evapotranspiration when it is not limited by fluid supply) is calculated as a complex function of temperature as given by Thornthwaite (1948). PE is then adjusted for the duration of daylight. Temperature variation data were made available by the Lisi meteorological station (see Fig. 3c), and the duration of daylight has been calculated by using a specific subroutine included in the WATBUG code (a code computing water budget in soil) of Willmott (1977). Soil moisture variation with time was calculated using a reservoir model and according to the procedure of Willmott (1977) in the WATBUG code. It assumes that, if precipitation P is less than PE, the water supplied is entirely

consumed by the evapotranspiration process and the surplus S is zero. The equation of Willmott (1977) in this case is somewhat different from (6). He suggested instead using

$$W_{t+1} = W_t + (P - PE) W_t / W_* , \tag{7}$$

where W_t is the soil moisture at time t and W_* is the water-holding capacity, which, briefly, is the water available for evapotranspiration within the whole soil layer. The higher W_* is, the greater the amount of evapotranspiration. The ratio W_t/W_* is called the extraction function.

If P is larger than PE, soil moisture varies as follows:

$$W_{t+1} = W_t + (P - PE) . \tag{8}$$

However, if $W_{t+1} > W_*$, then W_{t+1} is set equal to W_* and according to (6) the water surplus is given by $W_{t+1} - W_*$. This means that precipitation greater than the potential evapotranspiration is entirely absorbed by the change in storage, as long as soil moisture is lower than W_*.

Using these equations, we have been able to estimate the effective infiltration during the observation period at Lisi. An important point to note here is that precipitation includes both rainfall (Fig. 3d) and snowfall (Fig. 3e). Therefore, in addition to rainwater, snow melt is likely to infiltrate through the soil in the aquifer. Here we have to estimate the volume of fluid resulting from snow melt. Although it is quite a complex problem, we consider that it is only parametrized by temperature; we used a correspondence table (http://www.nws.noaa.gov/er/box/tables/snowfall-meltwater.html) that converts the snow cover into an equivalent water column. It is a rough estimate but sufficient for our purpose. Effective rainfall infiltration is given in Fig. 9 for comparison with Fig. 3(d). Bouwman *et al.* (1993) provided values of water-holding capacity for the top 30 cm of soil of the Georgian territory: depending on the location, the water-holding capacity is either 15 or 80 mm. However, it has been set equal to 30 mm in our modelling for reasons explained below.

Since the input function can now be estimated, we are able to proceed to the computation of the transfer function. We do not consider the smoothing of the input signal resulting from the flow of the fluid in the unsaturated zone. In other words, we assume that fluid transfer in the unsaturated zone is instantaneous and the transfer function that we compute includes the characteristics of transfer through the unsaturated zone.

Assuming that the transfer from the recharge area to the well is a linear process (implying that the medium is not too heterogeneous), water level $h(t)$ in the well is related to precipitation as follows:

$$w(t) = \Gamma(t) * s(t) , \tag{9}$$

where $w(t) = h(t) - r(t)$, $r(t)$ denotes the aquifer recession, that is, the decline of the water level when the input is zero, $\Gamma(t)$ is the transfer function, $s(t)$ is the input that corresponds to the surplus calculated above and the asterisk denotes the convolution product. Since we do not know the recession term, we write (9) as follows:

$$(h(t) - h_0) = \Gamma^*(t) * (s(t) - s_0) , \tag{10}$$

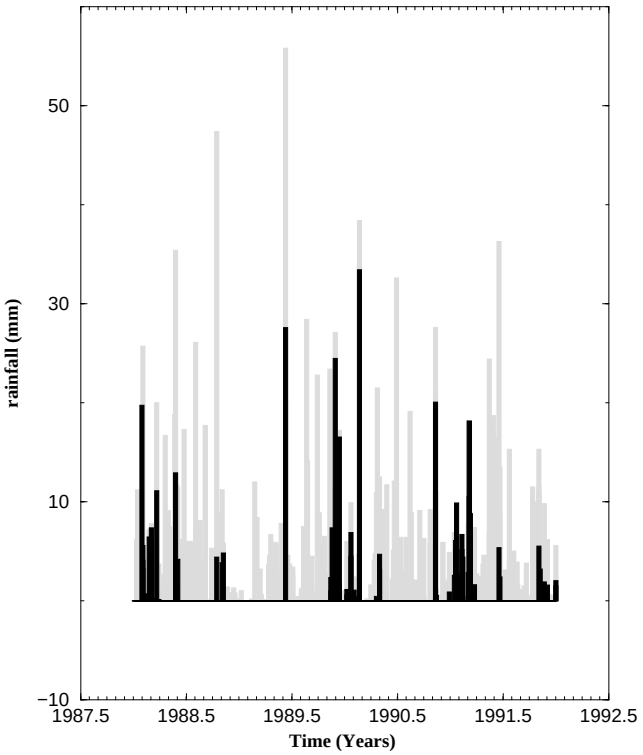

Figure 9. Comparison between the precipitation (grey) and infiltration (black).

where h_0 and s_0 are respectively the mean values of $h(t)$ and $s(t)$ over the observation period considered,

$$h_0 = 1/(t_f - t_0) \times \int_{t_0}^{t_f} h(t)\, dt ,$$

$$s_0 = 1/(t_f - t_0) \times \int_{t_0}^{t_f} s(t)\, dt ,$$

where t_0 and t_f are respectively the initial and final times. This simple assumption fixes the form of the recession curve with minor effects expected on the transfer function. This transfer function is denoted Γ^* in eq. (10), but in the following we identify $\Gamma^*(t)$ and $\Gamma(t)$. We are ready now to perform the deconvolution. This is done by assuming that $\Gamma(t)$ can be expressed as

$$\Gamma(t) = \frac{A_0}{(4\Pi c t)^{0.5}} \exp[-X^2/(4ct^{0.5})] + \sum_{K=1}^{K=N} A_k W_K^M(t) , \tag{11}$$

where c is the hydraulic diffusivity and A_i, $0 < i < N$, are constants. The first term of the expression corresponds to the solution of the diffusion equation for parallel flow and the second corresponds to a linear decomposition of an arbitrary function in Walsh functions W_K^M. This decomposition was suggested by Emsellem & de Marsily (1971). Subscript K refers to the nth-order Walsh function and superscript M corresponds to the length of the Walsh function, which fixes the memory size of the transfer function. This second term is likely to take account of the deviation from the parallel-flow standard solution. This may include various effects, in particular delay

and smoothing due to the infiltration through the unsaturated zone and possible complexities associated with the transfer pathways from the recharge area to the site of observation. Decomposition in Walsh functions provides a very flexible method of carrying out the deconvolution with minimal initial assumptions.

Although the Spitak earthquake signature is quite clear on the Lisi water level record, we first perform a blind deconvolution. This means that we perform a deconvolution on the whole record without considering possible anomalies related to earthquakes. The barometric and tidal components have been removed from the signal. However, as seen above, due to the dispersion of the barometric efficiency, the correction to the barometric effect is considered as rather poor.

As seen previously, the water-holding capacity has been set equal to 30 mm. Examination of residuals shows that this value gives the best fit to the data. It appears that although some discrepancies may be observed, the prediction matches the data reasonably well except during the period that follows the Spitak earthquake. Thus, using a blind deconvolution, an anomalous water level is observed for this time period.

The period of time over which deconvolution was applied is likely to contain anomalous regimes related to the earthquake. As a consequence, the transfer function might include information related to these anomalous regimes. Thus, we now perform deconvolution over a time period that is probably not affected by the earthquakes. The results are shown in Fig. 10(b). Transfer functions with or without the Walsh functions (see Fig. 10a) give rather similar results. However, since the Walsh functions do not contain any *a priori* assumptions about the shape of the transfer function, they are able to capture more detail and the prediction is better in this case. The memory of the transfer function is set equal to 512 days. Because such a memory may be seen as too large, smaller values have also been tested (e.g. 256), but this does not change the prediction significantly. Using these transfer functions, it appears that the predicted fluctuations of water level agree with observations for the entire period of observation, if one excepts a shift related to the Spitak earthquake (because the predicted signal is calculated in order to match the observed signal that follows the Spitak earthquake, the shift is apparent prior to the earthquake in Fig. 10b). Thus, in spite of large uncertainties in infiltration rate and in the geometry of the recharge/discharge system, a strong anomalous regime is highlighted after the Spitak event. We emphasize that we must distinguish long-term deviations from short-lived discrepancies between the predicted and observed signals. Short-lived discrepancies, of which the most characteristic example is given for the peak before the Racha earthquake, are probably due to the above-mentioned uncertainties. Considering that the general trend of the predicted signal (long-term variations) is rather good, the amplitude of local peaks may be poorly resolved. This highlights the limit of resolution of our method, which cannot capture events of short duration. On the other hand, the anomaly related to the Spitak earthquake seems to be a signal of long duration and leads to a global shift in water level after the Spitak event.

Subtracting the predictions from the observations, we are now able to estimate the water level anomaly associated with the Spitak earthquake. The trend of this anomaly is given in Fig. 11. This is restricted here to the 6 months that follow the earthquake. However, when considering the complete record, one observes that the initial water level is never recovered and, despite short-lived deviations, the water level anomaly remains constant for the whole period that follows the 6 months shown in Fig. 11 (that is, during the next 3 years). We fit the anomaly (for the whole of the recorded signal that follows the earthquake) using an exponential decay function. The water level decline due to the earthquake closely fits a function of the form

$$u(t) = u_0[1 - \exp(-t/t_e)], \tag{12}$$

where u_0 is 0.78 m and the time constant is $t_e = 6.65$ days. This is illustrated in Fig. 11. Using this function together with the transfer function shown in Fig. 10(a), we can now predict rather well the water level variation for the whole period of observation (Fig. 12). Water level heads result both from the infiltration (rain and snow) and from the earthquake response, which provides a permanent water level decline. This response is delayed in time with a time constant $t_e = 6.65$ days and one expects a permanent shift of 78 cm (at least on the timescale of the recording, that is, during the 3-yr-period that follows the earthquake). Using the exponential fit function makes it possible to compare our results with observations made by other authors. Roeloffs (1998) found $t_e = 0.5$ days for the Landers earthquake, whose epicentral distance was $\Delta = 433$ km and magnitude $M = 7.3$.

An important point to notice here is that the Racha earthquake does not provide any detectable anomaly either before or after the earthquake. Interestingly, we note that the strong peak before the Racha earthquake has been seen before as a precursor effect by Areshidze *et al.* (1992). In our opinion, this peak is related to snow melt (see Fig. 3e) and cannot be modelled without taking account of this process. Although the fit does not match the peak in Fig. 10(b) perfectly, this is probably mainly due to the poor estimation of snow melt infiltration. As pointed out before, the method provides only a rough approximation with regard to water level peak events. We may wonder if this discrepancy is likely to mask the earthquake-related anomalies. Since predicted water level matches rather well the observed value at the time of the Racha earthquake, we do not expect a strong effect on the long-term evolution of water level variation after the event.

3 MODELLING PHYSICAL PROCESSES

In this section we develop a model to provide an explanation for the observed anomalous signal. Since it is delayed in time, the anomaly cannot be attributed to the static coseismic deformation field. Moreover, according to the empirical formula for strain deformation given by Dobrovolsky (1991), it appears that the water level variation should not be higher that 13 cm. Roeloffs (1998) provided bases for analysing this kind of process. Following Rojstaczer *et al.* (1995), Roeloffs suggested that aquifer damage due to the passage of seismic waves could be responsible for permanent water level variations. The principal argument in favour of such a process lies in the prediction of the variation of water level by a function of the size and distance of the earthquake. It provides a lower bound for detectable water level variation that agrees with the observations. Moreover, expressing magnitude as a function of the amplitude of seismic waves and distance, Roeloffs derived the following expression: $\Delta h = A^{0.89} D^{-0.15}$. This indicates that water level variation should be dominated by the amplitude of seismic waves, that is, by the

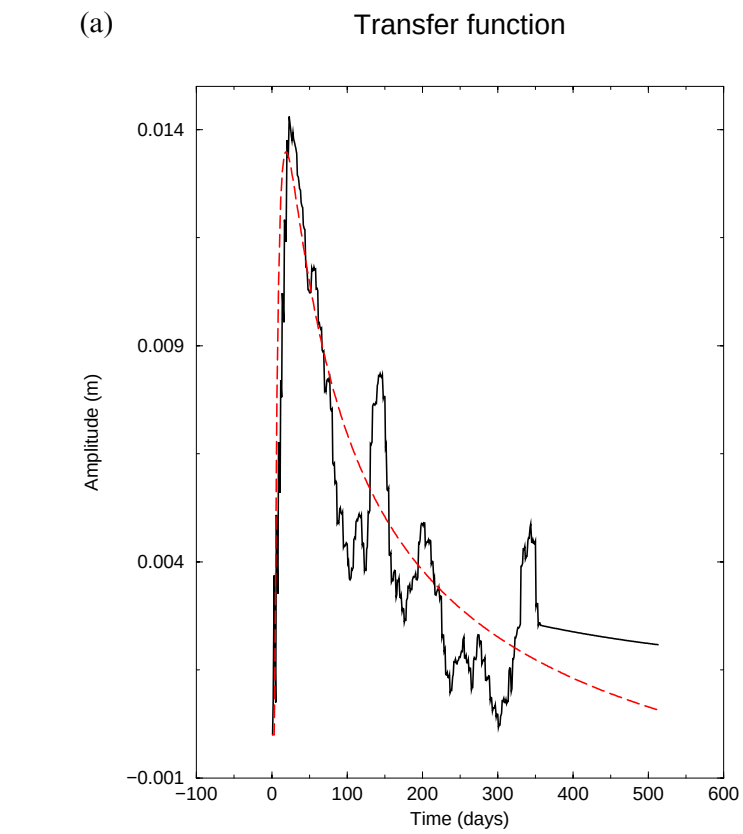

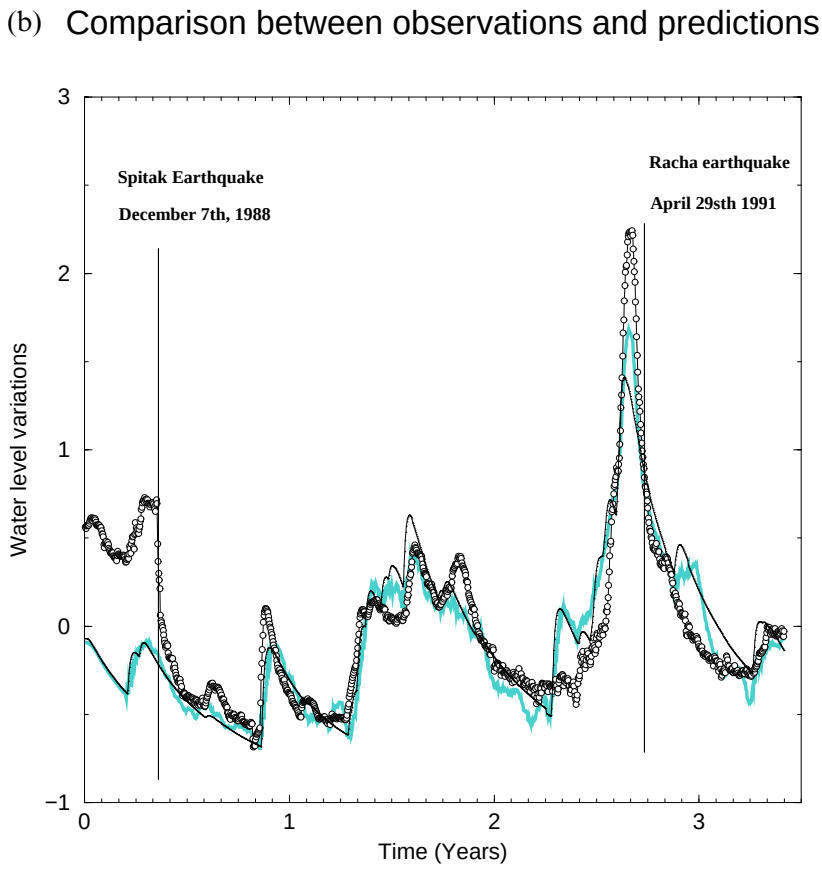

Figure 10. (a) Transfer function calculated from deconvolution with the Walsh function (solid line) and without the Walsh function (dashed line). (b) Predicted water level variations (thick grey line: with Walsh functions; thin black line: without Walsh functions) and observed variations (solid line with open circles).

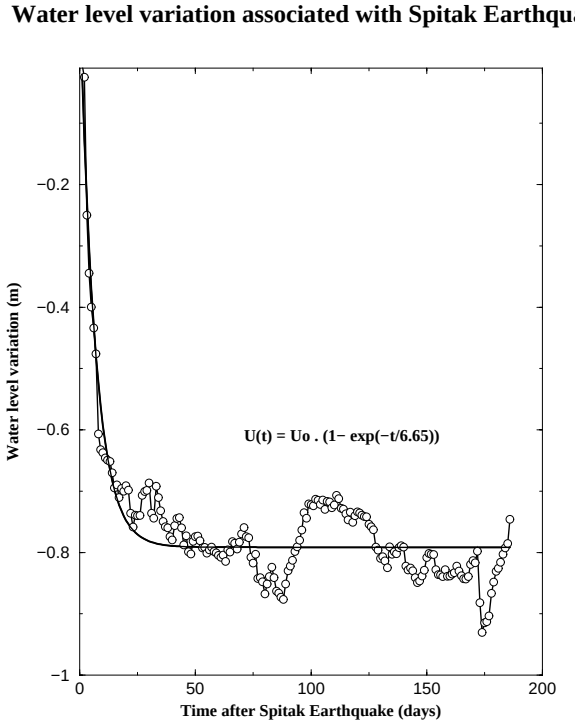

Figure 11. Water level anomaly versus time after the Spitak earthquake. Solid line with open circles: data. Solid line: best exponential fit. The amplitude is ≈ 0.78 m and the time constant is 6.6 days.

dynamic shear strain. According to this analysis, the damage associated with the passage of seismic waves is thus a plausible mechanism. We note, however, that the significant point, which is discussed hereafter, is that the aquifer undergoes an irreversible change, whatever the mechanism for this change. Nevertheless, since the Racha earthquake does not seem to provide an anomalous response, the mechanism considered should provide an explanation for this observation. The effects of directivity associated with the radiation pattern of surface waves should probably be considered. However, additional data are necessary to test this assumption further. With regard to this point, we are currently processing data from the 12 stations installed in the Western Caucasus during the observation period.

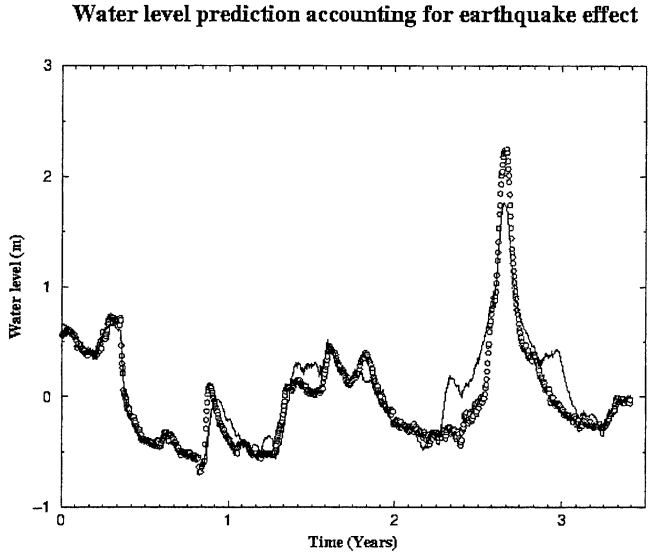

Figure 12. Same as Fig. 10(b), including the effect of the Spitak earthquake as shown in Fig. 11.

By retaining the passage of seismic waves as a possible mechanism for aquifer damage, we carry out some simple numerical tests that are useful in discriminating the various possible effects. Our goal here is not to describe all the complexity of the phenomenon, but rather to draw up a general framework of study.

We consider here only horizontal 2-D fluid flow. A schematic representation of the aquifer system is given in Fig. 13. The average aquifer length is set to $L = 6000$ m, from a local field map. Note, however, that since we do not know the exact flow path geometry at the Lisi site, this value may be a rough approximation. Nevertheless, the transfer function at a given distance X from the recharge area depends on the two quantities (L^2/c, X/L), where c is the diffusivity of the medium. With regard to modelling, it implies that at a given location X, the shape of the transfer function is known, provided that c and L are fixed. Thus, since c and L are not exactly known, they must be chosen in agreement with the derived transfer function. Nevertheless, provided that X, L and c are chosen in such a way that both quantities L^2/c and X/L remain constant, the shape of the transfer function would not change. As seen above, tidal analysis does not allow us to constrain very well the diffusivity, thus various possible values of (c, L) provide an adequate transfer function. However, even though L is not accurately known, field maps provide an order of magnitude estimate for aquifer length. We found that $L = 6000$ m (which is roughly consistent with the field map length measurement) and diffusivity associated with $K = 3 \times 10^{-7}$ m s^{-1} and $S_s = 0.26 \times 10^{-6}$ m^{-1} (i.e. $c = 1.15$ m^2 s^{-1}) as derived in the tidal analysis provide a transfer function at the location of Lisi that is consistent with the one derived above. Other pairs of values ($L = 7500$ m and $c = 1.8$ m^2 s^{-1}) may also be acceptable. However, it does not change the generality of what follows. Indeed, the time constant of water level relaxation associated with a given perturbation of the aquifer is well described as soon as the transfer function is adequately accounted for.

We used classic boundary conditions:

$$K \partial h/\partial x_{(x=L)} = \text{infiltration rate}, \tag{13}$$

$$h_{(x=0)} = 0, \tag{14}$$

$$\partial h/\partial y_{(\text{lateral boundaries})} = 0, \tag{15}$$

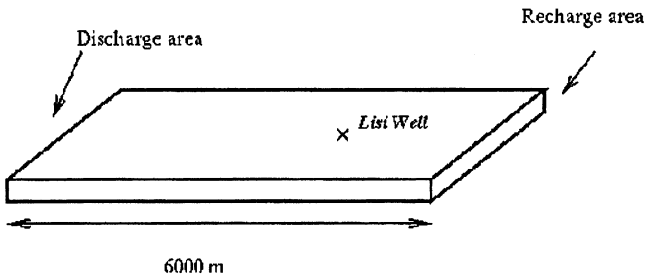

Figure 13. Schematic representation of the aquifer used in the numerical model.

where K is the hydraulic conductivity and h is the water level. In addition to spatial boundary conditions, conditions at $t=0$ are required. We simply consider that the aquifer is in state of equilibrium, that is, stationary fluid flow conditions are reached. According to eq. (10), if one neglects the pressure dependence of the hydraulic network, one obtains the following formula:

$$h(x,\, t=0)=(s_0K)x\,, \tag{16}$$

where, as above, s_0 is the average infiltration rate over the 3.5-yr-period of recording and K is the hydraulic conductivity.

3.1 Variable-permeability model

As noticed by Roeloffs (1998), a sharp increase (decrease) of permeability should be accompanied by a transient water level decrease (increase). The pressure equilibrium profile along the aquifer stabilizes at a new lower (higher) pressure gradient with a time constant that depends on the diffusivity of the medium. We used parameters consistent with those derived in the previous section for the aquifer and we compared the calculated response and the observed anomaly. Because the tidal analysis as well as the 'slug test' were performed following the earthquake, we consider that the hydraulic conductivity may have been lower before the earthquake and reached that estimated from tides after the event, i.e. $K=3\times10^{-7}$ m s^{-1}. In addition, S_s is set equal to 0.26×10^{-6} m^{-1}, which gives a diffusivity close to 1 m^2 s^{-1}. Doing that, we are now able to compare the theoretical response of the aquifer for various sets of ΔK and the observations. In Fig. 14 we show the anomaly that would result from an increase in hydraulic conductivity, starting from the initial value $K=1.475\times10^{-7}$ m s^{-1} up to the final value $K=3\times10^{-7}$ m s^{-1}.

Even though this value is only twice as high as the initial one, the final water level decline is consistent with the observations. On the other hand, the calculated time constant for aquifer relaxation, $t_r=150$ days, is much higher than t_e, and this has led us to reject it as the basic assumption of the model. Since the time constant is controlled by diffusivity, what happens when specific storativity is decreased by a factor of 20? In that case, the anomaly would be consistent with the observed anomaly. However, the transfer function would be strongly modified and would no longer be able to describe correctly the variation in the water level associated with rainfall.

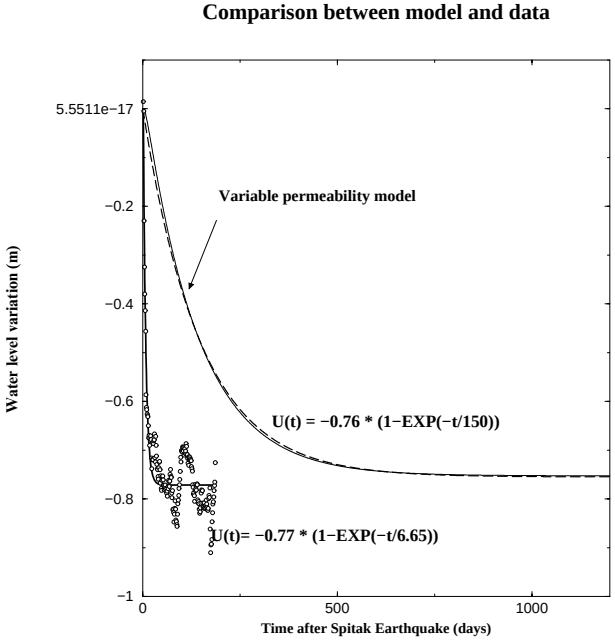

Figure 14. Comparison between observed anomaly (solid line with open circles) and that calculated from the 'variable-permeability model'.

3.2 Variable-porosity model

In the previous subsection we considered only permeability change. However, changes in both porosity and permeability may result from damage. In this subsection we consider the effect of porosity change. At first glance, it appears that porosity change cannot be uniformly distributed, otherwise pore pressure drop resulting from increased pore volume would be very fast. On the one hand, the time constant t_e is much lower than the aquifer relaxation time, t_r, but on the other hand, the process is not instantaneous either and is likely to include a process controlled by the diffusion of the fluid. Consequently, porosity variation could be localized and take place in some isolated blocks. In Appendix A, we describe the mathematical model that we used for describing local changes in porosity/permeability. It allows us to account for a coupling effect between fracturing and fluid flow. After the seismic waves pass, the localized damage is likely to occur at certain places in the aquifer. At the same time this induces changes in permeability and porosity, which are described in Fig. A1. Pressure drop caused by porosity variation is taken into account as well as fluid exchange between the initial matrix and the newly created porous volume. Disturbance due to the pore pressure drop is influenced both by the amplitude of the pressure drop (i.e. the porosity change) and by the dimension of the depressed zone. We present here some simulations that provide an idea of the expected response when one takes into account these variations of porosity. The geometry of the fractured zones is shown in Fig. 15. The shaded square zones correspond to the fractured zones and the shaded circular zones correspond to the various points of observation. As described in Appendix A, damaged zones

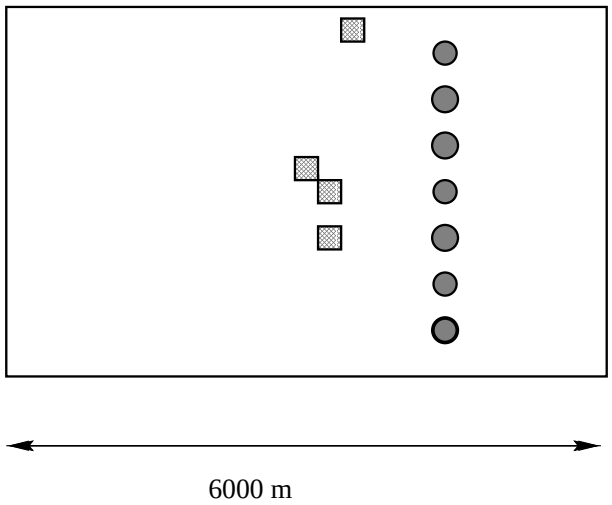

Figure 15. Schematic representation of the aquifer: the shaded squares correspond to the damaged zones and the shaded circles to the various observation points.

form a square network. The variation of porosity within the damaged zone is such that when equilibrium between pressure within the matrix and pressure within the fractures is reached, the water level decline is approximately 1.45 m. The porosity variation necessary to obtain this value is discussed below. The responses at the various points of observation are shown in Fig. 16. Although water level variation agrees rather well with observations for a short time period after the earthquake, the long-term behaviour is not compatible with a permanent water level decline. This behaviour is easy to understand if one considers the equilibrium equation, which depends only on the permeability if one assumes a rigid medium (see eq. 16). Modification of the storativity may also have an effect if pressure dependence of the hydraulic network were taken into account. However, since the variation of pressure is very weak and zones of porosity increase are very localized, one expects only a weak effect on the equilibrium profile of the fluid pressure. Thus, the return to equilibrium pressure is controlled by the diffusivity of the medium, and the disturbance due to the variation of porosity is a process of limited duration, as shown in Fig. 16. In conclusion, this mechanism is not able to describe the observations.

3.3 Towards a mixed model

As seen in the preceding paragraph, the 'variable-permeability' model is likely to describe the long-term behaviour of the aquifer (i.e. the permanent effect), whilst the 'variable-porosity' model could adequately describe the short-term behaviour. In this paragraph we suggest a mixed model that takes account of both permeability variation in the whole aquifer as described above and localized zones of porosity increase. Thus, at the time of the earthquake, we consider together the permeability increase as given in Section 3.1 and the porosity increase in localized zones as given in Fig. 15. Porosity increase is such that it leads to a water level decrease of 1.25 m within these zones. The resulting anomaly is given in Figs 17(a) and (b), where we compare the prediction of the mixed model with the data and with the prediction of the 'variable-porosity model', respectively. It appears that the variation of water level

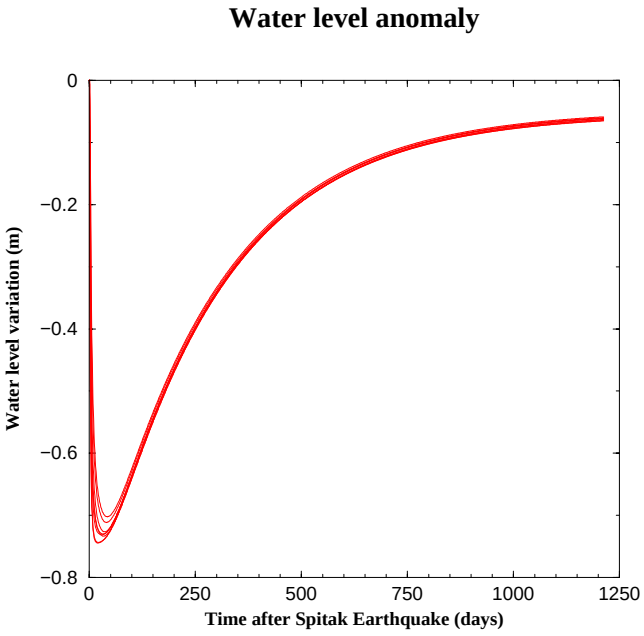

Figure 16. Water level anomaly associated with damage shown in Fig. 15 at the various observation sites. Referred to as the 'variable-porosity model' in the text.

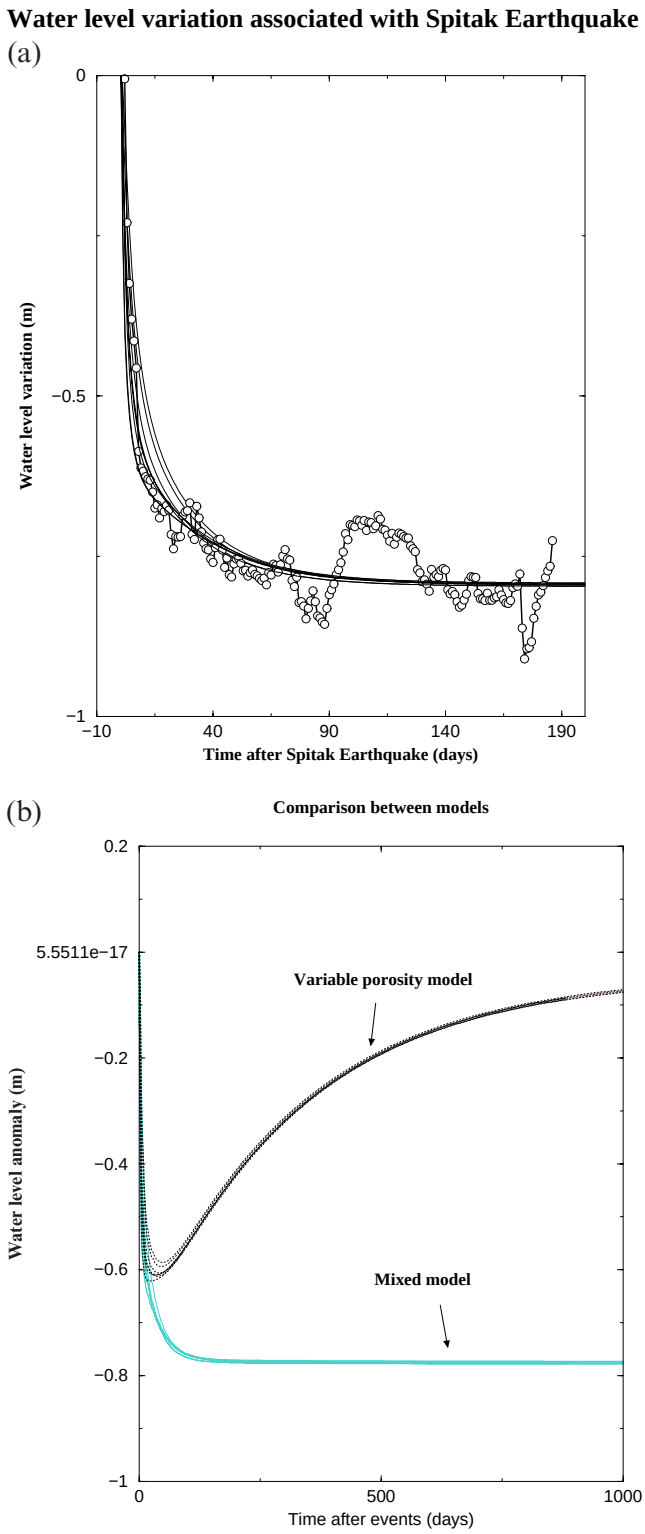

Figure 17. (a) Water level anomaly as expected from the 'mixed model' (solid line) and observed anomaly (solid line with open circles) for the first 6 months after the earthquake. (b) Comparison between the 'variable-porosity model' (dotted black lines) and the 'mixed model' (solid grey lines) for the whole period of observation.

associated with the earthquake is well described over the entire observation period. Starting from the initial water level profile, one can see that the porosity variation leads to a fast pressure drop that affects the surrounding areas and is responsible for the small time constants of the observed anomalies. The new position of equilibrium is then gradually reached. Finally, it is seen (Fig. 18) that the water level variation is fairly well described throughout the period of observation.

How do the positions of the various fractured zones affect the response at the points of observation? We now present two numerical simulations that provide brief answers to this question. Fig. 19 shows how the simulated anomaly varies when one gradually removes the fractured zones shown in Fig. 15. From this figure, it appears that the time constant of the water level decline results from the contributions of all the fractured zones. The more distant the fractured zones, the weaker their effect and the more this effect is delayed in time. Fig. 20 provides another viewpoint of this positioning effect. It shows the response at the various points of observation for another spatial distribution of fractured zones. Thinner dashed curves correspond to observation points closest to a fractured zone. Inverted peak-shaped curves are predicted in this case for the short time periods. To our knowledge, these peak-shaped curves have not yet been observed. Two reasons may be invoked to explain this. First, permanent water level declines following earthquakes are not ubiquitous in aquifers, and the characterization of the anomaly should cover a sufficient duration [if we restrict ourselves to an observation period of 10 days, the thin dashed

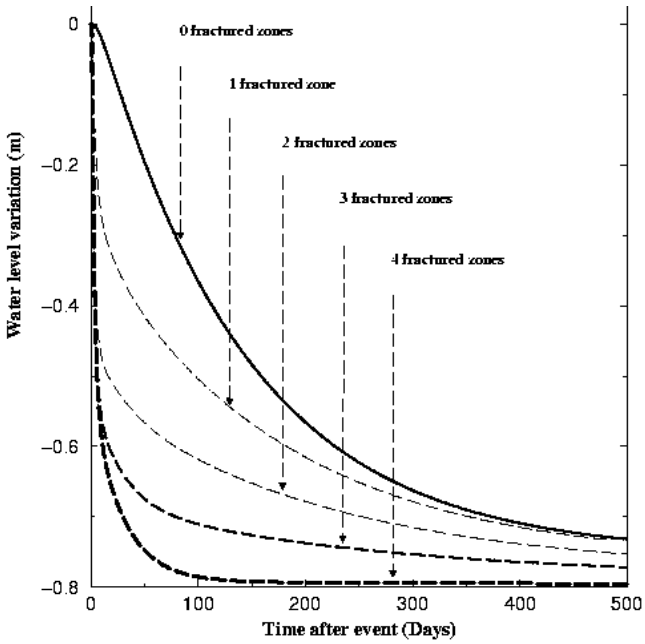

Figure 19. Evolution of the water level anomaly when removing the damaged zones (from the most distant to the nearest zone in Fig. 16).

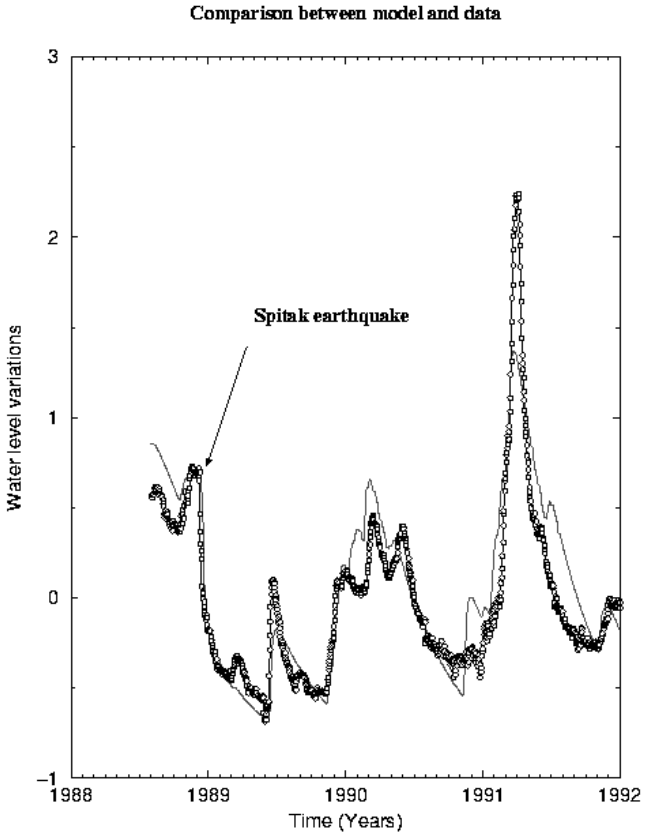

Figure 18. Predicted water level variation (solid line) starting from the 'mixed model'. The solid line with open circles corresponds to the data.

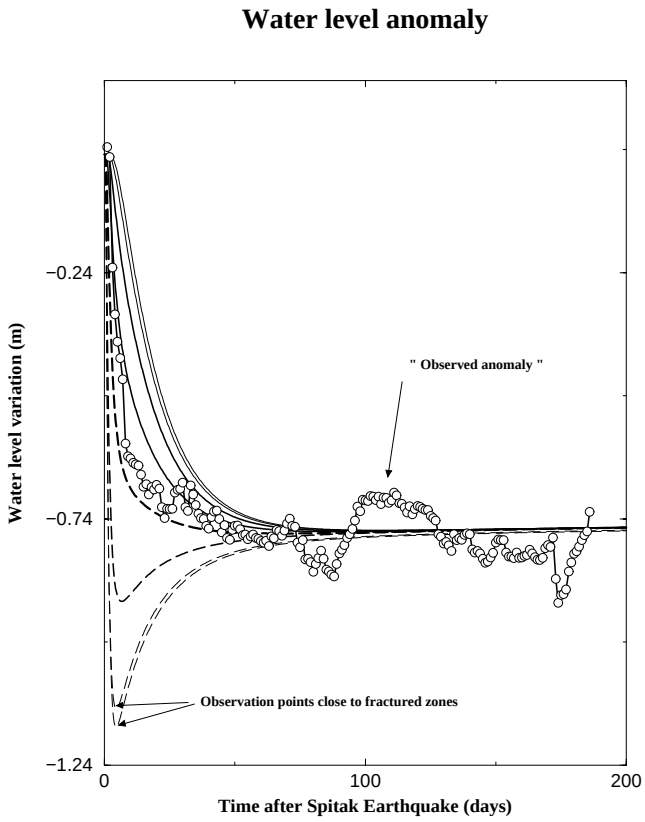

Figure 20. Water level anomaly for a particular spatial distribution of damaged zones at various observation sites. The solid line with open circles corresponds to the data.

curves of Fig. 20 display behaviour similar to that observed for the Northridge earthquake by Roeloffs (1998)]. Second, the lack of observation might have a probabilistic origin. Indeed, the probability for sampling close to a fractured zone might be rather weak. This effect would be enhanced if a 3-D model was considered.

4 DISCUSSION

In the preceding section, we saw that the mixed model describes the characteristics of the observed anomaly well. We recall that, according to the mixed model, permeability should increase to around twice its initial value. On the other hand, porosity increase in fractured zones is such that water level decline when equilibrium between fracture and matrix is reached is around 1.25 m. This last point needs some clarification. We consider a volume of fluid V_f and an average variation of volume ΔV_f. The porosity needed to reach the equilibrium pressure value is easily calculated from the following formula:

$$\Delta V_f / V_f = \rho g \Delta h \times \chi_f \,, \tag{17}$$

where χ_f is the coefficient of compressibility of the fluid. Setting $\chi_f = 5 \times 10^{-10}$ Pa^{-1}, one obtains $\Delta\Phi = 6.10^{-6} \times \Phi$, where Φ is the porosity. Although this value appears to be very low, one must keep in mind that whilst it corresponds to a spatial averaging on the volume of the macroscopic mesh, porosity variation is restricted to localized fractures (see Appendix A). The relative variation of volume within these fractures is then likely to depend on their spacing. It is easy to calculate the relative variation of volume within the fractures, $\Delta V_{frac}/V_{frac}$:

$$\Delta V_f / V_f = \Delta V_{frac}/V_f = (\Delta V_{frac}/V_{frac}) \times (V_{frac}/V_f)$$

and then

$$(\Delta V_{frac}/V_{frac}) = (\Delta V_f/V_f)/(V_{frac}/V_f) \,.$$

Thus, the relative variation of volume within the fracture varies with the fracture spacing as $(V_{frac}/V_f)^{-1}$. Of course it will depend not only on the spacing but also on the apertures of the fractures. We can handle this question by considering two end-member cases: either (1) the aspect ratio of fractures or (2) the permeability remains constant as fracture spacing varies. Fracture permeability varies as $K_f \propto w^3/l$ and fracture porosity as $\Phi_f \propto w/l$, where w is the aperture and l is the fracture spacing. According to these expressions, in (1) $\Delta V_{frac}/V_{frac} = \Delta V_f/V_f$ and does not depend on fracture spacing. In (2), $\Delta V_{frac}/V_{frac}$ scales as $(l/l_{min})^{2/3}$, where l_{min} is the characteristic size of the pores. For $l_{min} = 10^{-4}$ m and $l = 10$ m, one obtains $(\Delta V_{frac}/V_{frac}) \approx 0.01$. According to this simple calculation, whilst a very small porosity variation is required to model the observations, the relative variation of volume needed within the damaged 'pores' may be as large as 1 per cent.

Some points of discussion were avoided during the development of the model. The most questionable point concerns the damage associated with the passage of seismic waves. Thus, we need to answer the following questions.

4.1.1 Can seismic waves produce variations of porosity and permeability compatible with the requirements of the model?

The passage of seismic waves through the aquifer induces a dynamic cyclic loading on the fractures contained in the aquifer. The magnitudes of permeability and porosity variations are likely to depend strongly on the reorganization of the surface topography of fractures after shearing. This involves both mechanical and hydraulic effects. Laboratory experiments provide preliminary information on the processes that are involved.

Resistance to fracture slip is controlled by the coefficient of friction, μ. Depending on the range of values for the applied normal stress, the coefficient of friction may change. For a low normal stress (<200 MPa), as is the case here, Byerlee (1978) gives an average value $\mu = 0.85$. However, friction involves various microscopic processes and variables. For a low normal stress, the response of the fracture to shear loading is dominated by sliding over rough surfaces. Thus, the resistance depends on the angle between asperities and the sliding plane. Moreover, surface irregularities are responsible for the normal component of displacement, that is, for the dilatant behaviour, and for hysteresis under cyclic loading. This is the important point with regard to porosity and permeability variations. Going towards higher normal stress, shearing of asperities becomes easier than surface sliding. As a consequence, the dilatant behaviour is gradually less pronounced and degradation of asperities plays an increasing role. However, this has not yet been properly modelled. An important point to mention here is the distinction between matched and mismatched joints. The value for friction given by Byerlee (1978) was measured on matched joints. However, Byerlee (1967) showed that friction may have values as low as 0.15 for mismatched joints with smooth asperities. In addition, no significant dilatant behaviour is expected in this case.

With regard to dynamic loading, things are even less clear. According to Gilette *et al.* (1983), who performed measurements at frequencies varying from 0.001–10 Hz, joint strengths depends on the loading rate. The effect can be an increase or a decrease in friction according to the type of rock.

Let us return to our specific problem. At these distances the magnitude of dynamic stress may reach values around 1×10^5 Pa. It is likely to overcome the shear strength of joints in the upper aquifer. In the lower aquifer, whilst displacement may occur locally on asperity surfaces, macroscopic frictional sliding should not occur. The link with the hydraulic properties is still an unanswered question. Threshold effects within the fractures associated with the decorrelation of surfaces may induce a significant increase in permeability, although shear displacement is weak. Additional effects, including the shaking of material inside the fracture void space, should be taken into account in the modification of fluid transfer properties. However, these effects have not yet been well quantified.

4.1.2 Can the damage responsible for the global variation of permeability and that responsible for the zones of increased porosity coincide spatially?

The possibility that local damage induces a global modification of the permeability rests on the existence of a percolation threshold. If fractures within the aquifer are close to a threshold, percolation theory predicts a sharp variation of permeability even if a small number of fractures are added to the system. However, the problem here is that of a percolation of fractured zones embedded within a matrix permeability. Threshold effects are expected for contrasting values of fracture permeability (several orders of magnitude) compared to the initial matrix permeability. In our case, even in the most favourable configurations (in the proximity of the percolation threshold),

permeability variation associated with porosity variation would probably be small. If the two processes (permeability and porosity variations) take place, they are mainly uncoupled and we are then compelled to consider separate porosity and permeability variation mechanisms. Since both effects are likely to result from the same physical mechanism, i.e. seismic shaking, that they are uncoupled is rather surprising. The simplest explanation rests on the morphology of the surfaces of the fractures at various scales. Depending on their sizes, fractures are likely to react differently to dynamic sollicitations. Various hydrological effects are then expected according to the size of the fractures. However, further studies are needed to validate the basic assumption of the proposed model.

5 CONCLUSIONS

The appearance of an anomalous fluid regime following the Spitak earthquake has been highlighted. This anomaly is permanent. The amplitude of the drawdown is approximately 78 cm, a level that is reached with a time constant of 6.6 days. No clear anomaly was recorded at the time of the Racha earthquake.

The calibration of the parameters of the aquifer allowed us to discuss quantitatively the possible mechanisms responsible for this anomaly. A global increase of permeability by a factor of 2 is required to explain the long-term behaviour of the aquifer. The time constant of the anomaly would result from porosity increase within some localized zones.

The damage associated with the passage of seismic waves is seen as the physical process responsible for the modification of the aquifer parameters. However, this process is not well constrained and this indicates the need for additional field research under very well-constrained conditions. In particular, the monitoring of fracture zones under dynamic conditions would provide essential information in conjunction with long-term water level recordings.

ACKNOWLEDGMENTS

We are grateful for the careful and thoughtful review of E. Roeloffs. This work was supported by CNRS-INSU through the PNRN project 'Dynamic of earthquakes: physical models'. PG wishes also to thank S. Pride for his help. Special thanks to H. P. Valero and F. Touchard for their strong encouragement throughout this study.

REFERENCES

Areshidze, G. *et al.*, 1992. No preseismic evidence from hydrogeochemical parameters on the occasion of the April 29, 1991, Georgian earthquake, Caucasus, *Tectonophysics,* **213,** 353–358.

Bendat, J.S. & Piersol, A.G., 1986. *Random Data: Analysis and Measurement Procedures,* J. Wiley, New York.

Bouwman, A.F., Fung, I., Matthews, E. & John, J., 1993. Global analysis of the potential for N_2O production in natural soils, *Global biogeochem. Cycles,* **7,** 557–597.

Bredehoeft, J., 1967. Response of well-aquifer-systems to earth tides, *J. geophys. Res.,* **72,** 3075–3087.

Byerlee, J.D., 1967. Theory of friction based on brittle failure, *J. appl. Phys,* **38,** 2928–2934.

Byerlee, J.D., 1978. Friction of rocks, *Pure appl. Geophys,* **116,** 615–626.

Dobrovolsky, I.P., 1991. *Mechanika Podgotowki Tectonisheskowo Semletrjasenia,* Nauka, Moscow (in Russian).

Domenico, P.A. & Schwartz, F.W., 1990. *Physical and Chemical Hydrogeology,* J. Wiley, New York.

Douglas, J. & Arbogast, T., 1990. Dual porosity models for flow in naturally fractured reservoirs, in *Dynamics of Fluids in Hierarchical Porous Media,* pp. 177–222, ed. Cushman, J.H., Academic Press, London.

Emsellem, Y. & de Marsily, G., 1971. An automatic solution for the inverse problem, *Water Resources Res.,* **7,** 1264–1283.

Gilette, D., Sture, S., Ko, H.-Y., Gould, M.C. & Scott, G.A., 1983. Dynamic behaviour of rock joints, in *Proc. 24th US Symp. on Rock Mechanics.*

Hsieh, P.A., Bredehoeft, J.D. & Farr, J.M., 1987. Determination of aquifer transmissivity from earth tide analysis, *J. geophys. Res.,* **72,** 3075–3087.

Hvorslev, M.J., 1951. Time lag and soil permeability in groundwater observations, *Waterways Experiment Station Corps of Engineers US Army Bull.,* Vicksburg, MS.

Igarashi, G. & Wakita, H., 1991. Tidal responses and earthquake-related changes in the water level of deep wells, *J. geophys. Res.,* **96,** 4269–4278.

Kumpel, H.J., 1992. About the potential of wells to reflect stress variations within inhomogeneous crust, *Tectonophysics,* **211,** 317–335.

Muir-Wood, R. & King, G.C.P., 1993. Hydrological signatures of earthquake strain, *J. geophys. Res.,* **98,** 22 035–22 068.

Papadopoulos, I.S., Bredehoeft, J.D. & Cooper, H.H., 1973. On the analysis of slug test data, *Water Resources Res.,* **9,** 1087–1089.

Roeloffs, E., 1988. Hydrologic precursor to earthquakes: a review, *Pure appl. Geophys.,* 177–209.

Roeloffs, E., 1998. Persistent water level changes in a well near Parkfield, California, due to local and distant earthquakes, *J. geophys. Res.,* **103,** 869–889.

Roeloffs, E. & Quilty, E., 1997. Water level and strain changes preceding and following the August 4, 1985 Kettleman Hills, California, earthquake, *Pure appl. Geophys.,* **149,** 21–60.

Roeloffs, E., Budford, S.S., Riley, F.S. & Records, A.W., 1989. Hydrological effects on water level changes asssociated with episodic fault creep near Parkfield, California, *J. geophys. Res.,* **94,** 12 387–12 402.

Rojstaczer, S., 1988. Intermediate period response of water levels in wells to crustal strain: sensitivity and noise level, *J. geophys. Res.,* **93,** 13 619–13 634.

Rojstaczer, S., Wolf, S. & Michel, R., 1995. Permeability enhancement in the shallow crust as a cause of earthquake-induced hydrological changes, *Nature,* **373,** 237–239.

Roosbeek, F., 1996. RATGP95: a harmonic development of the tide generating potential using an analytical method, *Geophys. J. Int.,* 197–204.

Thornthwaite, C.W., 1948. An approach toward a rational classification of climate, *Geograph. Rev.,* **38,** 55–94.

Willmott, C.J., 1977. Watbug: a Fortran IV algorithm for calculating the climatic water budget, *Publ. Climatol.,* **30,** 2–4.

APPENDIX A: MODELLING COUPLED FLUID FLOW AND FRACTURING

Modifications of the hydraulic network may generate variations of both permeability and specific storativity (and in particular, porosity change). Transient effects will thus depend on the pore pressure drop associated with the porosity change, the redistribution of fluid mass and the modification of the hydraulic regime due to the aquifer damage (either global or local). We need modelling tools that include some information (even if crude) on the geometry of damage and that can account for the coupled effect between irreversible modification of the

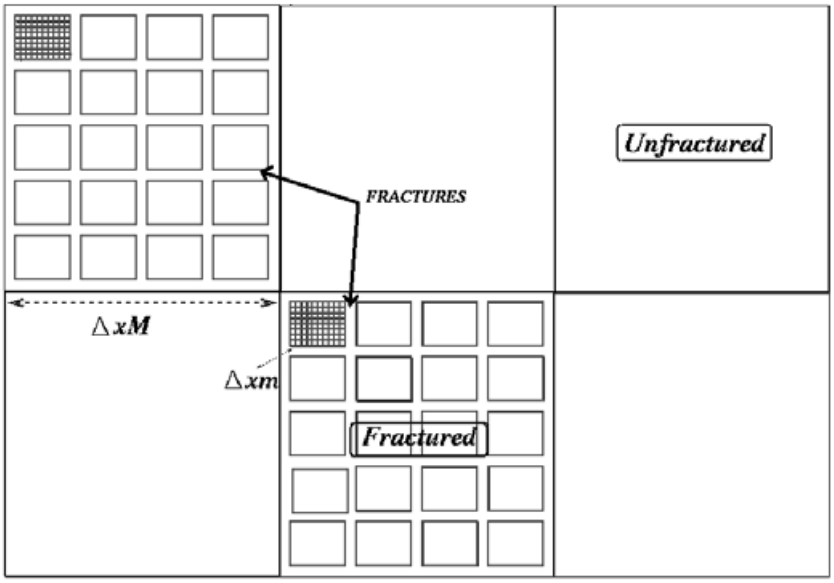

Figure A1. Schematic representation of the discretization scales used in the double-porosity model. Δx_M is the macroscopic scale. Δx_m is the microscopic scale.

porous network and fluid pressure. We will consider that the reactivated fractures may be seen as a second porous phase with specific hydraulic properties that differ from the matrix properties. Keeping in mind these assumptions and simplifications, we have to deal with a damaged aquifer that may be seen at least locally as a double-porosity medium.

We adopt here the description and numerical scheme given in Douglas & Arbogast (1990), modified to account for porosity change within the fractured phase. Fluid flow in the fractured network is expressed as follows:

$$S_f \frac{\partial(P_f)}{\partial t} = \nabla[(K_f/\eta)\nabla P_f] + Q_{ext} + Q_m\,, \tag{A1}$$

where P_f is the fluid pressure within fractures, S_f and K_f are respectively the specific storage and the permeability of the fractured system, η is the flow viscosity, Q_{ext} contains all the external sources, including water supplied in the system and irreversible porosity changes, and Q_m is the fluid mass exchanged with the matrix per unit time. It may be expressed by the following formula:

$$Q_m = -\sum_i \frac{1}{\Omega_i} \int_{\Omega_i} \frac{\partial(\Phi_m \rho_m)(\xi, t)}{\partial t}\, d\xi\,, \tag{A2}$$

where the subscript i corresponds to a summation on the matrix blocks whose volume is Ω_i and which are contained within the volume unit, Φ_m is the porosity of the matrix and ρ_m is the density of the fluid within the matrix. Fluid flow within each matrix block is expressed by

$$S_m \frac{\partial(P_m)}{\partial t} = \nabla[(K_m/\eta)\nabla P_m]\,, \tag{A3}$$

where P_m is the fluid pressure within the matrix block and S_m and K_m are the specific storage and the permeability of the matrix block, respectively. In addition, boundary conditions are expressed at the interface between the block and the surrounding fractures. The two discretization scales we used are schematically represented in Fig. A1. Δx_M is the macroscopic grid spacing, which includes a finite number of matrix blocks. These blocks are discretized according to the microscopic grid size Δx_m. Readers interested in the algorithm for solving the coupled equations (A1) and (A2) are referred to Douglas & Arbogast (1990). When fracturing occurs we have to consider porosity and permeability changes. Although fracturing is expected to be an instantaneous process, we considered that porosity increases linearly over a given time period T_r, mainly to avoid numerical problems. As long as a quasi-static problem is considered, the choice of T_r has no impact on calculations, provided it is short. A good criterion would be $T_r \ll T_m$, with T_m the time constant for diffusion within the matrix block (that is, half of the fracture spacing). In that case, a quasi-undrained behaviour is expected. In practice, larger rise times still give acceptable results.